Exploring the Stability of Mixed Halide Vacancy Ordered Quadruple Perovskites

Matthew B. Gray^, Jackson D. Majher^, Noah P. Holzapfel, and Patrick M. Woodward*

Department of Chemistry and Biochemistry, The Ohio State University, 100 W. 18th Avenue, Columbus, Ohio 43210, United States

Abstract

The structural and optical properties of the halide substitutions of Br^- and I^- into $Cs_4M^{II}M^{III}_2Cl_{12}$ ($M^{II} = Cd^{2+}$, Mn^{2+} and $M^{III} = Bi^{3+}$, Sb^{3+}) have been investigated. All compositions adopt the <111> layered vacancy ordered quadruple perovskite structure with $R\bar{3}m$ space group symmetry. Through incremental halide substitution reactions, we show that significant bromide incorporation is possible (>25% for Cd^{2+} containing structures). The larger halide ions (Br^- or I^-) preferentially occupy the anion sites adjacent to the cation-vacancy layer. In those compositions where M^{II} is Cd^{2+}, incorporation of bromide ions leads to substantial M^{II}/vacancy antisite disorder, which is accompanied by a more even distribution of bromide substitution over the two chemically distinct anion sites. The $Cs_4CdM^{III}_2Cl_{12}$ compounds can incorporate over twice the amount of bromide as analogous Mn^{2+} containing compounds, with a maximum of 29(2)% bromide substitution found for $Cs_4CdSb_2Cl_{12}$. Iodide incorporation is more limited, with a maximum of ~6% halide substitution for $Cs_4CdBi_2Cl_{12}$. The incorporation of the heavier, less electronegative Br^- and I^- ions results in a red shift of the onset of optical absorption in a Vegard's Law type fashion. The effect is largest for $Cs_4CdBi_2Cl_{12-z}X_z$, where the absorption onset shifts from 3.20(1) eV to 2.99(1) eV as the composition changes from $Cs_4CdBi_2Cl_{12}$ to $Cs_4CdBi_2Cl_{8.9}Br_{3.1}$. As discussed in the paper these results offer some insights into the factors that stabilize the vacancy ordered quadruple perovskite structure.

Introduction

Halide perovskites with the general formula AMX_3 ($A = CH_3NH_3^+$, Cs^+; $M = Pb^{2+}$, Sn^{2+}; $X = Cl^-$, Br^-, I^-) have been researched intensively in recent years, due to their promise as inexpensive, high-efficiency solar absorbers for photovoltaic applications. Since the initial 2009 report, power conversion efficiencies have skyrocketed to an impressive 25.5%.[1,2] Furthermore, quantum dots of lead halide perovskites, $APbX_3$, are attractive electroluminescent materials for LEDs as they are highly tunable and have excellent color purity.[3] Yet another field rapidly advancing from halide perovskite research is the development of down-converting phosphors for phosphor converted light emitting diodes (pc-LEDs).[4]

Simple perovskites are highly amenable to chemical substitution and can often support significant concentrations of vacancies. For example, replacing the M^{II} octahedral cation with a 2:1 mixture of a trivalent cation and a vacancy results in a related phase, $Cs_3M^{III}_2Br_9$ ($M^{III} = Sb^{3+}$ or Bi^{3+}), where layers of corner connected M^{III}-centered octahedra are separated by layers of cation vacancies, leading to a two-dimensional (2-D) perovskite derivative. Interestingly, this structure type can also be accessed via the solid solutions $Cs_3Bi_2Cl_{9-x}I_x$ and $Cs_3Sb_2Cl_{9-x}I_x$ despite the respective end members having crystal structures that are different from the bromide analogue.[5–7] Halide substitution in these systems leads to the larger, less electronegative anion preferentially substituting onto the site adjacent to the vacancy layers.

Cation ordering can also be used to convert the prototypical $AM^{II}X_3$ perovskite into a $A_2M^IM^{III}X_6$ double perovskite, by replacing two M^{II} cations with a M^I and M^{III} cation pair in a three-dimensional (3-D) checkerboard pattern. This structure typically maintains the cubic symmetry of the perovskite archetype, but rock salt ordering of cations changes the space group from $Pm\bar{3}m$ to $Fm\bar{3}m$. Double perovskites have attractive optical and optoelectronic properties, while providing an avenue to eliminate toxic Pb^{2+}.[8–11]

The vacancy ordered quadruple perovskites (VOQPs) are a relatively new addition to the family of perovskite related structures. These structures, which take the general formula $A_4M^{II}\nu M^{III}_2X_{12}$ (ν = vacancy, $X = F^-$, Cl^-), arise from ordering of M^{II}/M^{III} cations and vacancies into layers that run perpendicular to the <111> direction of the cubic double perovskite structure.[12,13] Among the various physical properties of VOQPs, photoluminescence appears to

be the most promising for applications.[13–19] We recently demonstrated bright, orange-red photoluminescence in the $Cs_4Cd_{1-x}Mn_xBi_2Cl_{12}$ system, with a 57% photoluminescent quantum yield (PLQY) at room temperature.[17] Given the absence of rare-earth ions, good chemical stability, and ease of synthesis, this is a promising new phosphor. For use in pc-LEDs, the limiting feature is the excitation maxima ($\lambda_{max} \approx 360$ nm), which is too far into the UV to efficiently pair with a blue LED excitation source. Previous results studying the double perovskite $Cs_2NaBiCl_6:Mn^{2+}$ show that partial substitution of bromide for chloride can red-shift the excitation profile,[11] a desirable feature we explore here.

Among reported chloride VOQPs, the A-site is typically a cesium ion. Two rubidium based VOQPs have been reported, but they are extremely moisture sensitive.[15] The M^{III} site is either Sb^{3+} or Bi^{3+}; both possess a ns^2 valence electron configuration that seems critical in stabilizing the layered VOQP structure. Thus far, VOQPs have been reported with Mn^{2+}, Cu^{2+}, and Cd^{2+} occupying the M^{II} site.[14,16] The reasons why other divalent first row transition metals cannot be incorporated into the structure is not entirely clear. The anions in previously synthesized VOQPs are almost exclusively chloride, with $K_4Fe^{2+}Fe^{3+}{}_2F_{12}$ being a notable exception.[12] The incorporation of chloride or fluoride anions results in large band gaps and limits optical tunability, features that can be limiting for optoelectronic applications. The preparation of bromide VOQPs would expand the potential for tuning the optoelectronic properties of these materials. For example, bromide incorporation in $Cs_4MnBi_2Cl_{12}$ may serve to shift the excitation energy towards the range of visible light LEDs. Various calculations on the stability of $Cs_4CdBi_2Br_{12}$ and $Cs_4CdSb_2Br_{12}$ have come to different conclusions. Xu et al. predicted that $Cs_4CdSb_2Br_{12}$ and several $Cs_4M^{II}Bi_2Br_{12}$ phases should be stable with respect to decomposition into CsBr, $M^{II}Br_2$ and $Cs_3Bi_2Br_9/Cs_3Sb_2Br_9$.[20] Hu et al. questioned the validity of these predictions because some key ternary decomposition products were overlooked.[21] This concern seems founded based on earlier calculations by Lin et al., who found both $Cs_4CdSb_2Br_{12}$ and $Cs_4CdBi_2Br_{12}$ unstable with respect to decomposition into $CsCdBr_3$ and $Cs_3Bi_2Br_9/Cs_3Sb_2Br_9$.[16] Thus far, neither of these bromide VOQP phases have been synthetically realized, partially motivating the current study. Here, we explore the incorporation of heavier halides (Br^- and I^-) into several VOQPs to probe the phase stability and better understand the behavior and limits of bromide and iodide substitution into the VOQP structure.

Experimental

The vacancy ordered quadruple perovskites, $Cs_4M^{II}M^{III}_2Cl_{12-z}X_z$ ($M^{II} = Cd^{2+}$, Mn^{2+}, $M^{III} = Bi^{3+}$, Sb^{3+}, $X = Br^-$, I^-), were synthesized through precipitation from an aqueous solution of concentrated HCl(*aq*) (Fisher Scientific, 37%), phosphinic acid (H_3PO_2, Sigma Aldrich, 50 wt. % in H_2O), and either HBr (Alfa Aesar, 47–49%) or HI (Sigma Aldrich, 47+%) depending on the targeted composition. For a typical 2.00 g synthesis of $Cs_4CdSb_2Cl_{12}$, 0.196 g (1.52 mmol) of CdO (Cerac, 99.95%) and 0.444 g (1.52 mmol) of Sb_2O_3 (Acros, 99+%) were added to a ~15 mL vial. To this, 10 mL of HCl and 1 mL H_3PO_2 were added under stirring conditions at room temperature. Once dissolved, the reaction was triggered by the addition of 1.026 g (6.09 mmol) CsCl (Alfa Aesar, 99%) and allowed to vigorously stir for 1 hour. This solution was dried via vacuum filtration, then washed with minimal 2-propanol (Fisher Scientific, Certified ACS Plus) and allowed to dry overnight. To promote halide substitution and form $Cs_4CdSb_2Cl_{12-z}X_z$ ($X = Br^-$, I^-), systematic aliquots of either HBr or HI were added to the reaction vessel prior to the addition of phosphinic acid. The volumes of HBr(*aq*)/HI(*aq*) added ranged from 0.15 mL to in excess of 2 mL, while the volumes of HCl and H_3PO_2 were kept fixed. $Cs_4CdBi_2Cl_{12-z}X_z$, $Cs_4MnBi_2Cl_{12-z}X_z$, and $Cs_4MnSb_2Cl_{12-z}X_z$ ($X = Br^-$, I^-) were synthesized via the same protocol, using Bi_2O_3 (Alfa Aesar, 99.99%) in place of Sb_2O_3 and/or $MnCl_2{\cdot}4H_2O$ (Mallinckrodt, 99%) in place of CdO as appropriate.

Powder X-ray diffraction (PXRD) data were collected on a Bruker D8 Advance powder diffractometer (40 kV, 40 mA, sealed Cu X-ray tube) equipped with a Lynxeye XE-T position-sensitive detector. The data were collected with an incident beam monochromator (Johansson type SiO_2-crystal) that selects only Cu $K\alpha_1$ radiation ($\lambda = 1.5406$ Å). Rietveld refinements of laboratory PXRD data were carried out using the TOPAS-Academic (Version 6) software package to determine the crystal structure.[22]

UV-visible diffuse reflectance spectra (DRS) were collected from 178–890 nm with an Ocean Optics USB4000 spectrometer equipped with a Toshiba TCD1304AP (3648-element linear silicon CCD array). The spectrometer was used with an Ocean Optics DH-2000-BAL deuterium and halogen UV−vis−NIR light source and a 400 μm R400-7-ANGLE-VIS reflectance probe. The detector was calibrated using a Spectralon Diffuse Reflectance Standard.

Results

Crystal Structure

Before discussing the results of the halide substitution reactions, it is important to understand the terminology that will be used to describe VOQPs. The ideal VOQP has sheets of corner-sharing M^{III}–M^{II}–M^{III} octahedra separated by layers where the octahedral sites are vacant. This layered structure has two halide positions: a halide ion that bridges the M^{III} and M^{II} octahedra, and a halide ion that is adjacent to the vacancy layer and bonds only to the M^{III} ion (Figure 1). The M^{II} cation resides on the 3a Wyckoff site, while the vacancy is on the 3b Wyckoff site. In some compositions a percentage of the M^{II} cations populate the vacancy layer. When substantial, this M^{II}/vacancy antisite disorder blurs the distinction between the two halide sites and leads to an electronic structure that is intermediate between 2-D and 3-D. Nevertheless, for the sake of simplicity we will refer to the halide adjacent to the 3a Wyckoff site as the bridging site, and the halide adjacent to the 3b Wyckoff site as the terminal site, even when there is antisite disorder. Figure S1 shows the VOQP structure with varying amounts of antisite disorder, highlighting the increase in dimensionality. It should be noted that a larger $Fd\bar{3}m$ cell has also been reported for some VOQPs.[16] Our experiments have only resulted in the rhombohedral structure, but this does not rule out the possibility that the cubic structure could form under appropriate synthetic conditions.

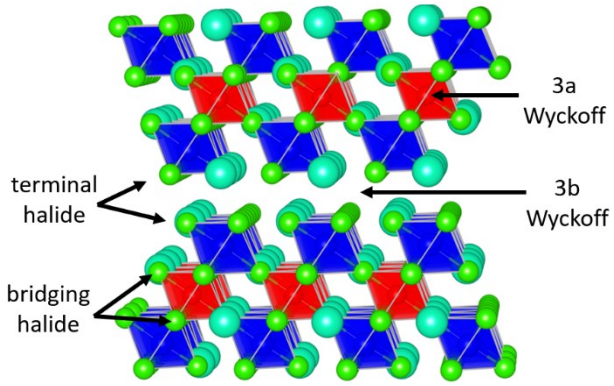

Figure 1. Crystal structure of the $Cs_4M^{II}M^{III}_2Cl_{12}$ VOQP with the bridging and terminal halide positions depicted. In the absence of M^{II}/vacancy antisite disorder, the 3a Wyckoff site is fully occupied and the 3b Wyckoff site is vacant. The Cs^+ ions are shown in cyan, M^{II} in red, M^{III} in blue, and Cl^- in green.

All chloride VOQPs synthesized, $Cs_4M^{II}M^{III}_2Cl_{12}$ ($M^{II} = Cd^{2+}$, Mn^{2+}, $M^{III} = Bi^{3+}$, Sb^{3+}), crystallize into the layered structure shown in Figure 1, with $R\bar{3}m$ symmetry. The unit cell parameters are consistent with previous reports.[15,17] Partial substitution of the chloride site with heavier halide ions ($X = Br^-$, I^-) results in an expansion of the unit cell, while maintaining the $R\bar{3}m$ structure. Figures S2–S9 shows the PXRD patterns for systematic bromide or iodide substitution into various $Cs_4M^{II}M^{III}_2Cl_{12}$ ($M^{II} = Cd^{2+}$, Mn^{2+}, $M^{III} = Bi^{3+}$, Sb^{3+}) compositions. In each case increasing substitution results in peak shifts to lower 2θ, signifying an expansion of the unit cell dimensions. For most cases, the ratio of Br^-/I^- to Cl^- was higher in the substituted VOQP crystals than in the solution from which they were prepared, suggesting a thermodynamic driving force for the heavier halide ions to incorporate into the VOQP structure, up to a certain limit (Figure 2). The cell volume increases linearly with the amount of Br^-/I^- in the reaction mixture (Figures S10 and S11), as expected given the larger radii of these ions.

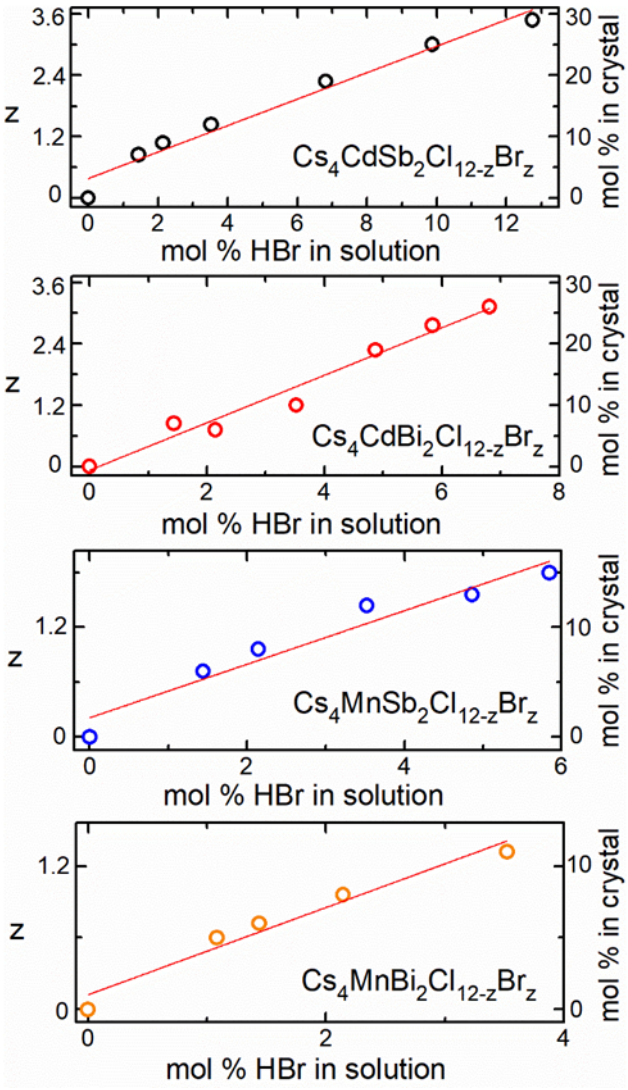

Figure 2. Bromide incorporation into various $Cs_4M^{II}M^{III}_2Cl_{12-z}Br_z$ compositions as a function of mol % HBr in solution.

Two ordering schemes for VOQPs ($R\bar{3}m$ or $Fd\bar{3}m$) are possible and were considered when analyzing the PXRD data.[17] Structural refinements from powder diffraction data show that rhombohedral symmetry is observed for all samples studied here. Interestingly, $Cs_4CdSb_2Cl_{12}$ shows an increase in the Cd^{2+}/vacancy antisite disorder as the bromide incorporation increases. However, analysis of the diffraction pattern does not suggest a unit cell that is metrically cubic; peak splitting of certain reflections is observed, which can only be accounted for with the $R\bar{3}m$ structure (Figure S12 and S13). Rietveld refinement allows for the determination of the halide occupancies due to the contrasting X-ray scattering power of the halide ions. A representative refinement of a $Cs_4CdBi_2Cl_{12-z}Br_z$ sample prepared in 1000 µL HBr is shown in Figure S14. No

additional peaks are observed following bromide incorporation. Interestingly, analysis of peak broadening in the PXRD patterns show minimal strain broadening, unlike an earlier study of $Cs_2AgBiCl_{6-x}Br_x$ double perovskites.[23] The remaining Rietveld refinements for the samples that show the highest halide substitutions for each $Cs_4M^{II}M^{III}_2Cl_{12-z}X_z$ composition are shown in the Supporting Information (Figure S15–S20, Table S1–S3). Preferential occupancy of the terminal halide position that resides next to the vacancy layer is observed for the heavier anions, as illustrated for the bromide substituted systems in Figure 3.

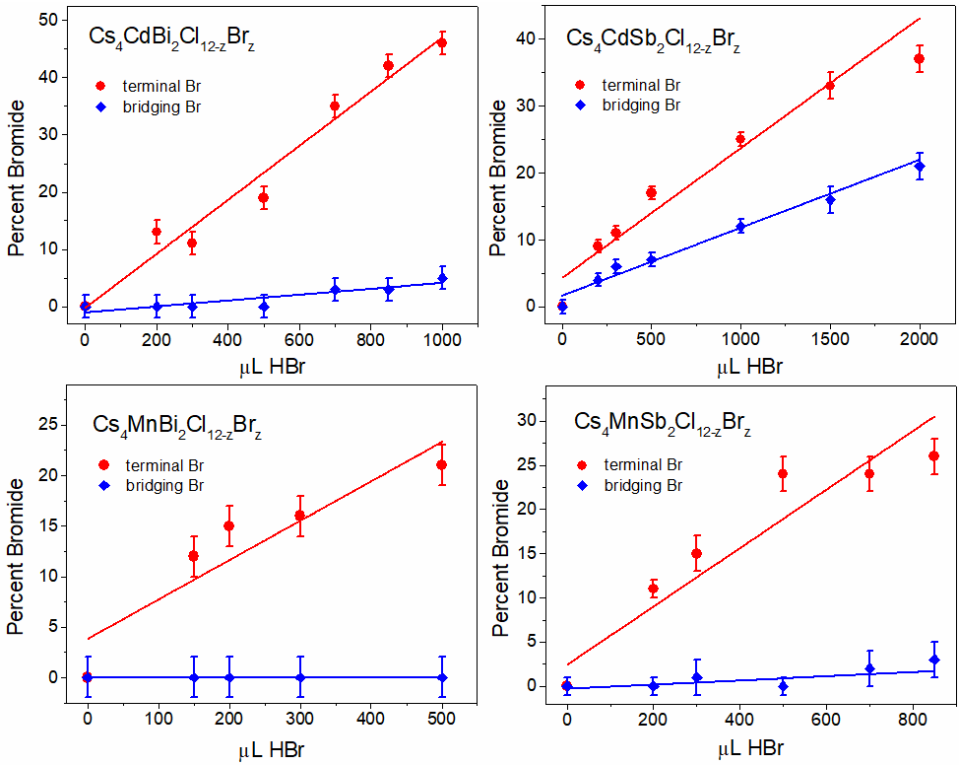

Figure 3. The refined site occupancy of bromide ions in $Cs_4CdM^{III}_2Cl_{12-z}Br_z$ and $Cs_4MnM^{III}_2Cl_{12-z}Br_z$ (M^{III} = Bi^{3+}, Sb^{3+}). Lines are guides for the eye.

The volumetric expansion of the unit cell in response to halide substitution is expected given the radii of the halide ions. Iodide more rapidly expands the volume because it has a larger crystal radius than bromide (2.06 Å vs. 1.82 Å). However, we observe that a larger mole fraction of bromide can be incorporated. These effects are illustrated in Figure 4. By either measure, the amount of the heavier halide ion that can be incorporated is significantly larger when the M^{II} ion is Cd^{2+} than it is when it is Mn^{2+}. Over twice the volume expansion occurs for the cadmium

containing systems in comparison to the manganese analogues. Rietveld refinements show that cadmium containing systems can incorporate up to 3.5 bromide ions per formula unit (i.e. $Cs_4CdM^{III}_2Cl_{8.5}Br_{3.5}$), whereas the maximum concentration of bromide ions in the manganese-containing compositions is only half that value (i.e. $Cs_4MnSb_2Cl_{10.2}Br_{1.8}$). Iodide substitution levels are significantly less in all hosts, ranging from 5.8(6)% of the total anion content in $Cs_4CdBi_2Cl_{12}$ to 1(1)% in $Cs_4MnBi_2Cl_{12}$. These results are summarized in Table S1 and refined halide occupancies for all compounds are given in Tables S2 and S3.

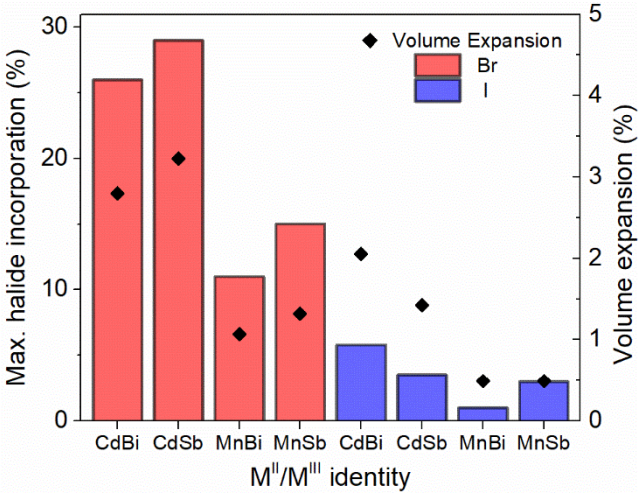

Figure 4. Bar graph showing the percentage of all anions that are either Br^- or I^- in maximally substituted samples. The unit cell volume expansion of maximally substituted samples with respect to the unsubstituted $Cs_4M^{II}M^{III}_2Cl_{12}$ samples are indicated with filled diamonds. Both values were obtained from Rietveld refinements of X-ray powder diffraction data.

The maximum amount of halide incorporation in each system is governed by the stability of the possible side phases that can form in solution. These phases have been identified and are listed with lattice parameters in the Supporting Information (Table S4). When the heavier halide ion is bromide, the layered $Cs_3Bi_2Br_9$ structure (a vacancy ordered variant of the cubic perovskite structure) competes with the VOQP structure at high Br^- substitution levels, though the lattice parameters indicate that these phases are better described as $Cs_3M_2Br_{9-x}Cl_x$ ($M = Sb^{3+}$, Bi^{3+}) with substantial levels of Cl^- incorporation. For substitution reactions involving iodide, the $Cs_3Bi_2I_9$ structure, which contains dimers of face-sharing octahedra (a vacancy ordered variant of the 6H perovskite structure), is observed, despite the existence of a stable layered $Cs_3M_2Cl_{9-z}I_z$

compound.[5,7] An exception to this trend is observed in the $Cs_4MnBi_2Cl_{12-z}I_z$ series, in which the layered $Cs_3Bi_2Br_9$ structure is observed. In the $Cs_4MnBi_2Cl_{12-z}X_z$ ($X = Br^-, I^-$) systems an additional side phase is identified, $CsMnCl_3{\cdot}(H_2O)_2$. This phase has not been considered as a decomposition product in previously published computational modeling of $Cs_4MnM^{III}{}_2Cl_{12}$ VOQP phase stability, as most thermodynamic decomposition calculations do not consider the possible formation of hydrated phases.

The optical properties of the bromide and iodide substituted VOQPs were studied via UV-vis DRS. The reflectance data, transformed to pseudo-absorbance using the Kubelka-Munk (KM) function by $\alpha = (1-R)^2/2R$, where α is the optical absorption coefficient and R is the reflectance. The changes in absorption onset as a function of halide substitutions are represented in Figure 5. All diffuse reflectance and resulting KM data for bromide and iodide substitution reactions are available in the SI (Figure S21).

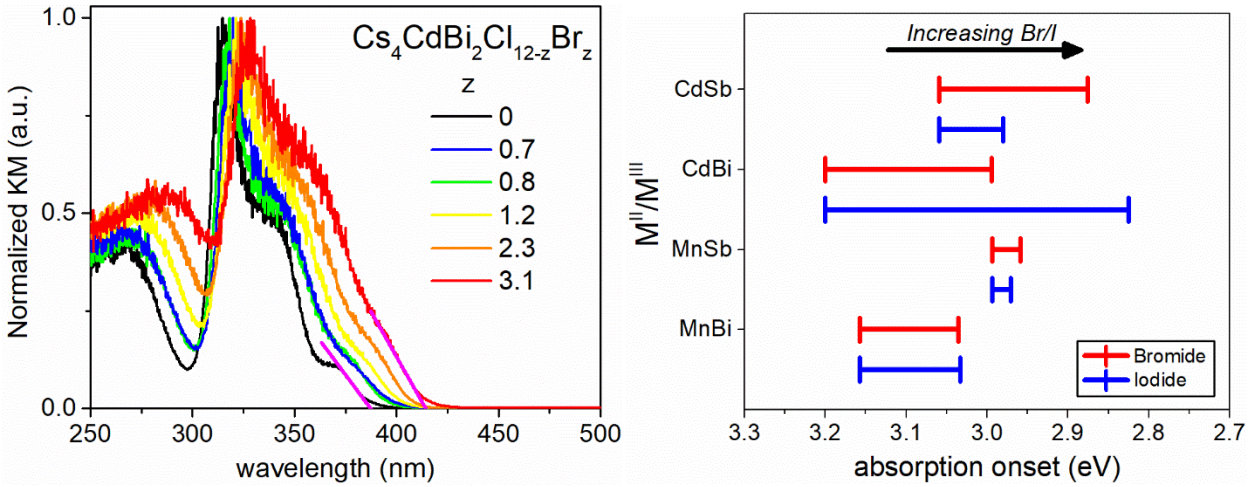

Figure 5. (Left) Kubelka-Munk transformation of diffuse reflectance data for $Cs_4CdBi_2Cl_{12-z}Br_z$; the extrapolated absorption onsets are given by magenta lines. (Right) The range of absorption onset for each $Cs_4M^{II}M^{III}{}_2Cl_{12-z}Br_z$ (red) and $Cs_4M^{II}M^{III}{}_2Cl_{12-z}I_z$ (blue) solid solutions. In each system, the onset of absorption shifts to lower energy as z increases.

As seen in Figure 5, incorporation of Br^- into the structure leads to a progressive red shift of the absorption onsets. For $Cs_4CdBi_2Cl_{12-z}Br_z$, the lowest energy onset is observed to shift from 3.20(1) eV to 2.99(1) eV as the Br^- content reaches its maximum value of 26(2)%. Bromide incorporation shifts the absorption characteristics of the VOQPs to lower energies due to the decreased electronegativity of bromide in comparison to chloride. This shifts the valence band

upward, as the higher energy regions of the valence band are predominantly halide *p*-orbital in character.[16] The ability to manipulate the band gap through halide substitution is common in halide perovskites and is a useful feature for optoelectronic applications. Qualitatively similar shifts to smaller band gaps are seen in all systems investigated. The effect is not as large in the Mn-containing systems, because less bromide can be incorporated. Although only relatively small amounts of iodide can be incorporated in the VOQP structure, this substitution can produce shifts in the band gap that are comparable to samples with higher levels of bromide substitution.

Discussion

This study was motivated in part by a desire to red shift the absorption onset and photoluminescent excitation (PLE) maxima to make the VOQPs more practical for photovoltaic and/or photoluminescent applications. The results show a red-shift in absorption can be obtained for all systems, with the most significant shifts occurring in the $Cs_4CdBi_2Cl_{12-z}X_z$ ($X = Br^-, I^-$) systems. Unfortunately, the absorption onset is >2.8 eV in all cases, still too large for even tandem solar cell devices. The rationale behind red-shifting the PLE spectrum via halide substitution is based on previous studies of $Cs_2NaBiCl_{6-x}Br_x:Mn^{2+}$, which showed a ~21 nm (~185 meV) red shift in PLE upon ~10% bromide incorporation. Earlier studies of $Cs_4MnM_2Cl_{12}$ ($M = Sb^{3+}, Bi^{3+}$) found PLE maxima near 355 nm.[15,17] In the present study, halide substitution caused a dramatic decrease in photoluminescent intensity, making measurement of the PLE unreliable for all systems investigated. It would appear the disorder inherent to mixed Cl^-/Br^- compositions enhances nonradiative return to the ground state. This could be alleviated if $Cs_4M^{II}M^{III}_2Br_{12}$ VOQPs could be stabilized, but the results of this study indicate that pure bromide VOQPs are inherently unstable. This observation is corroborated by calculations on relative enthalpies of formation of bromide VOQPs with respect to mixtures of binary and/or ternary phases.[16] Let us take a closer look at what factors inhibit the formation of bromide and iodide VOQPs and limit the number of cations that can be used in chloride VOQPs.

Formulaically, a VOQP with stoichiometry of $A_4M^{II}M^{III}_2X_{12}$ can be obtained by combining $AM^{II}X_3$ and $A_3M^{III}_2X_9$ phases (Figure 6b). Computations indicate that for $Cs_4CdM^{III}_2X_{12}$ ($M^{III} = Sb^{3+}, Bi^{3+}$; $X = Cl^-, Br^-$) compositions either the VOQP phase ($X = Cl^-$) or a 1:1 combination of $CsCdX_3$ and $Cs_3M^{III}_2X_9$ ($X = Br^-$) has the lowest energy of any combination of competing

phases.[16] Therefore, it is instructive to examine the structure stabilizing forces that are operative in the competing $AM^{II}X_3$ and $A_3M^{III}_2X_9$ compositions.

The observed crystal structures of $RbM^{II}X_3$ and $CsM^{II}X_3$ compositions are given in the SI (see Table S5). There are a handful of cubic perovskites ($RbCdF_3$, $RbMnF_3$, $RbFeF_3$, and $CsCdF_3$) and distorted variants of this structure ($RbCdCl_3$ and $RbCuF_3$), but most compositions adopt one of the so-called hexagonal perovskite structures. Whereas a cubic perovskite can be described as cubic close packing (ccp) of AX_3 layers with the M cations filling octahedral holes that are not adjacent to an A cation (the 3C structure, Figure 6c), hexagonal perovskites have varying degrees of hexagonal close packing (hcp) of AX_3 layers, which leads to the presence of face sharing MX_6 octahedra. In the 6H structure there is a 2:1 ccp to hcp ratio and dimers of face sharing octahedra are formed as a result (Figure 6e). The 9R structure features a 1:2 ccp to hcp ratio and trimers of face sharing octahedra (Figure S22).[24] The 2H structure adopts a 100% hcp sequence and infinite chains of face sharing octahedra (Figure 6g).

For oxides, fluorides, and chlorides the most stable $AM^{II}X_3$ structure is generally governed by the tolerance factor *t* (Equation 1)

$$t = \frac{r_A + r_X}{\sqrt{2}(r_M + r_X)} \quad (1)$$

where r_A, r_M and r_X are the ionic radii of A, M and X, respectively. The cubic structure is generally found to be most stable when *t* is near unity. When *t* is significantly larger than unity hexagonal structures are typically seen. As the tolerance factor increases the fraction of hcp increases, leading to the progression 3C (smallest *t*) < 6H < 9R < 2H (largest *t*). This general trend holds for $AM^{II}Cl_3$ and $AM^{II}F_3$ compounds, as evidenced by the fact that $CsCdCl_3$ and $CsMnF_3$ are both 6H, while $RbCdCl_3$ and $RbMnF_3$, which have smaller tolerance factors, are both 3C. The progression from 6H for $CsCdCl_3$ ($t = 0.95$) to 9R for $CsMnCl_3$ ($t = 0.99$) to 2H for $CsMCl_3$ ($M = Fe^{2+}$, Co^{2+}, Ni^{2+}; $1.01 < t < 1.04$) is also in line with expectations based on the sizes of the ions involved.

Upon moving to the larger, more polarizable bromide and iodide anions the 2H structure emerges as the most stable AMX_3 structure, regardless of the size of the M^{II} ion. This behavior cannot be explained by the tolerance factor, as it can be shown that increasing the size of the anion, while keeping the sizes of the cations constant, results in a decrease in *t* (Figure S24).

Instead, it is more likely that the preference for the 2H structure is related in some way with the increasing polarizability of the halide ion. In the cubic perovskite structure, the M–X–M bonds are linear, and this symmetric geometry leads to minimal polarization of the electron clouds on the halide ions. In contrast, the face-sharing octahedra that define the 2H structure give rise to M–X–M bonds that are closer to 90°. In this geometry the smaller M^{II} ions are on the "same side" of the halide ion and therefore work cooperatively to polarize its electron cloud. Madden and Wilson have shown that anion polarization effects such as this are critical to stabilization of layered structures among alkaline earth halides with heavier halide ions, such as CaI_2 and $MgBr_2$, both of which crystallize with the CdI_2 structure.[25]

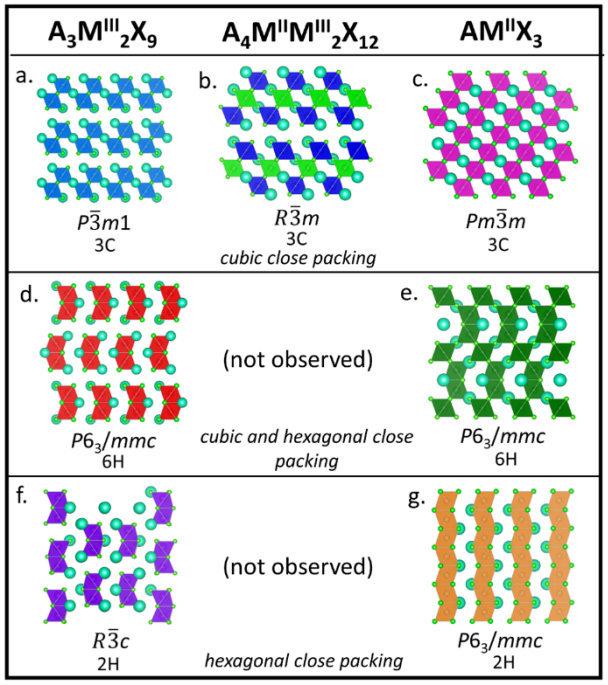

Figure 6. Visualization of observed crystal structures for perovskite and vacancy ordered perovskites with M^{II} and M^{III} ions. The relationship between structures is shown by their corresponding AX_3 packing sequences.

The crystal chemistry of $Cs_3M^{III}_2X_9$ phases has many parallels to that of the $AM^{II}X_3$ compositions described above. The layered structure of $Cs_3Sb_2Br_9$ and $Cs_3Bi_2Br_9$ with $P\bar{3}m1$ symmetry is a vacancy ordered derivative of the 3C cubic perovskite structure (Figure 6a). Both $Cs_3Sb_2I_9$ and $Cs_3Bi_2I_9$ crystallize with a structure that is analogous to the 6H structure with vacancies on those octahedral sites that only share corners with neighboring octahedra.[26] The shift from a structure with corner-sharing octahedra and ~180° M–X–M bonds for the bromides to a structure with face-sharing octahedra and ~90° bonds for the iodides may be driven by anion

polarization effects. The crystal structures of $Cs_3M^{III}_2Cl_9$ chlorides depends upon the nature of the M^{III} ion. When the M^{III} ion has a stereoactive lone pair (Sb^{3+}, Bi^{3+}) a structure with zig-zag chains of corner-sharing octahedra and a mixture of ccp and hcp stacking of CsX_3 layers is observed (Figure S23), although metastable polymorphs with the layered $P\bar{3}m1$ polytypes can also be stabilized at room temperature. When the M^{III} ion is a smaller transition metal ion (Cr^{3+}, Fe^{3+}) the vacancy ordered 6H derivative with $P6_3/mmc$ symmetry is observed (Figure 6d), whereas for larger M^{III} ions (M^{III} = Sc, Y, Tl) a vacancy ordered derivative of the 2H structure with $R\bar{3}c$ symmetry is seen (Figure 6f). The latter two structures are seen for a variety of $Cs_3M^{III}_2Br_9$ and $Cs_3M^{III}_2I_9$ phases, but importantly the layered $P\bar{3}m1$ with cubic close packing of CsX_3 layers is only seen with M^{III} is a lone pair cation (As^{3+}, Sb^{3+}, Bi^{3+}) and the anion is either bromide or chloride.

Understanding these structural preferences helps to explain the limited range of compositions that can be incorporated into the VOQP structure. The presence of a lone pair cation on the M^{III} site seems to be critical, much as it is for stabilizing the layered $P\bar{3}m1$ structure of $Cs_3M_2Br_9$ (M^{III} = Bi^{3+}, Sb^{3+}). It is well established in the literature that the driving force behind development of a stereoactive electron lone pair distortion tends to decrease as the electronegativity of the anion decreases.[27] It is possible that the introduction of the less electronegative Br^- or I^- anions reduces the lone pair distortions of $Sb^{3+}$and Bi^{3+} and thereby destabilizes the VOQP structure. To maintain the cubic close packing of the VOQP structure, it is important that the M^{II} ion not be too small, which may explain why researchers have not been able to make $Cs_4M^{II}M^{III}_2Cl_{12}$ phases with M^{II} = Fe^{2+}, Co^{2+}, Ni^{2+}, all of which are smaller than Mn^{2+} or Cd^{2+}.[15] Finally, as the polarizability of the anion increases the ~180° M–X–M bond angles seen for the bridging anions appear to become increasingly unfavorable. This may also explain the strong preference of the more polarizable bromide and iodide ions for the terminal halide positions adjacent to the vacancy layer. In fact, in the absence of antisite disorder between the M^{II} ion and the vacancy sites, the substitution levels of bromide and iodide ions on the bridging anion site are minimal. A similar preference for the heavier halide ion to avoid the bridging sites is seen for layered perovskite derivatives, including the mixed halide $Cs_3M^{III}_2X_9$ (M^{III} = Bi^{3+}, Sb^{3+}) phases and the all-inorganic $Cs_2PbI_2Cl_2$ Ruddlesden-Popper phase.[7,28]

Interestingly, $Cs_4CdSb_2Cl_{12}$ shows less of a preference for terminal halide site occupancy, which can be rationalized by analyzing the antisite disorder in this system. As bromide is added into the system, the antisite disorder increases linearly reaching a maximum of 23(2)% (Figure S25). It seems likely that the presence of substantial antisite disorder helps to alleviate two-coordinate bridging geometry for the halide ions that occupy the intralayer sites.

We can extrapolate the findings of this study to make some predictions about compositions that might lead to new VOQPs. Use of smaller A^+ cations (e.g. Rb^+) may help to reduce the tolerance factor that comes with smaller M^{II} ions (e.g. Fe^{2+}, Co^{2+}, Ni^{2+}) thereby alleviating local bond strains that destabilize the ccp stacking of the VOQP structure. While the prospects for finding VOQP based entirely on bromide or iodide anions are not promising, there is reason to believe that new VOQP phases containing the less polarizable fluoride ion might be found. In fact, there is a published example of a layered fluoride VOQP, $K_4Fe^{2+}Fe^{3+}{}_2F_{12}$ where the Fe^{3+} ion occupies the site normally occupied by Bi^{3+} or Sb^{3+}.[12] We should also note that there are some examples of oxide VOQP phases with high valent d^0 ions like W(VI) or Re(VII) on the sites where we find Sb^{3+} and Bi^{3+} in the chloride phases.[29] That both types of ions can undergo 2nd order Jahn–Teller distortions to alleviate bond strains associated with cation-vacancy ordering is likely not a coincidence.

Conclusion

The results reported here show the ability to tune the VOQP structure and absorption profile by partial halide substitutions. These compounds all crystallize into the layered VOQP structure and the lattice volume linearly increases as the larger halide is incorporated. In $Cs_4CdBi_2Cl_{12}$ and $Cs_4CdSb_2Cl_{12}$ a significant fraction of the chloride ions can be replaced with bromide, with substitution percentages of 26(2)% and 29(2)%, respectively. Rietveld analysis shows that the heavier, more polarizable bromide and iodide ions preferentially occupy the terminal positions adjacent to the vacancy layer. Incorporation of bromide changes the absorption profile, with the $Cs_4CdBi_2Cl_{12-z}Br_z$ system showing a ~200 meV red shift. A survey of structural driving forces for VOQP formation sheds light on the structure stabilizing factors that must be considered to understand and predict new VOQP compositions. This analysis suggests that the incorporation of less polarizable anions, such as fluoride or oxide, is likely to lead to new materials.

ASSOCIATED CONTENT

Supporting Information

The Supporting Information is available free of charge on the ACS Publications website.

(Figure S1) Antisite visualization for VOQPs. (Figure S2) Stacked PXRD of $Cs_4CdBi_2Cl_{12-z}Br_z$. (Figure S3) Stacked PXRD of $Cs_4CdSb_2Cl_{12-z}Br_z$. (Figure S4) Stacked PXRD of $Cs_4MnBi_2Cl_{12-z}Br_z$. (Figure S5) Stacked PXRD of $Cs_4MnSb_2Cl_{12-z}Br_z$. (Figure S6) Stacked PXRD of $Cs_4CdBi_2Cl_{12-z}I_z$. (Figure S7) Stacked PXRD of $Cs_4CdSb_2Cl_{12-z}I_z$. (Figure S8) Stacked PXRD of $Cs_4MnBi_2Cl_{12-z}I_z$. (Figure S9) Stacked PXRD of $Cs_4MnSb_2Cl_{12-z}I_z$. (Figure S10) Lattice volume increase with HBr addition. (Figure S11) Lattice volume increase with HI addition. (Figure S12) Comparison of $R\bar{3}m$ and $Fd\bar{3}m$. (Figure S13) Rietveld refinement of $Cs_4CdSb_2Cl_{12}$:2000 μL HBr. (Figure S14) Rietveld refinement of $Cs_4CdBi_2Cl_{12}$:1000 μL HBr. (Figure S15) Rietveld refinement of $Cs_4MnBi_2Cl_{12}$:500 μL HBr. (Figure S16) Rietveld refinement of $Cs_4MnSb_2Cl_{12}$:850 μL HBr. (Figure S17) Rietveld refinement of $Cs_4CdBi_2Cl_{12}$:250 μL HI. (Figure S18) Rietveld refinement of $Cs_4CdSb_2Cl_{12}$:200 μL HI. (Figure S19) Rietveld refinement of $Cs_4MnBi_2Cl_{12}$:70 μL HI. (Figure S20) Rietveld refinement of $Cs_4MnSb_2Cl_{12}$:200 μL HI. (Table S1) Rietveld refinement summary. (Table S2) Cell volume, HBr amount, percentage halide incorporation. (Table S3) Cell volume, HI amount, percentage halide incorporation. (Table S4) Side phases found upon VOQP breakdown. (Figure S21) Diffuse reflectance and Kubelka–Munk data. (Table S5) Structure type and tolerance factors for simple halide perovskites. (Figure S22) 9R crystal structure. (Figure S23) Crystal structure of $Cs_3Bi_2Cl_9$. (Figure S24) Tolerance factor of single perovskites for different halides. (Figure S25) Antisite disorder changes in $Cs_4CdSb_2Cl_{12-z}Br_z$. (PDF).

Acknowledgements

Funding was provided by the National Science Foundation under award number DMR-2003793.

AUTHOR INFORMATION

Corresponding Author

*E-mail: woodward.55@osu.edu

ORCID

Matthew B. Gray: 0000-0002-9526-4732

Jackson D. Majher: 0000-0002-4160-4201

Noah P. Holzapfel: 0000-0002-4566-4033

Patrick M. Woodward: 0000-0002-3441-2148

Author Contributions

^These authors contributed equally. M.B.G. and J.D.M. conceived of the project. M.B.G. synthesized and characterized all bromide substituted materials. J.D.M. synthesized and characterized all iodide substituted materials. N.P.H. modeled and analyzed the crystallographic data. P.M.W. sourced funding and supervised the work. The manuscript was written through contributions of all authors. All authors have given approval to the final version of the manuscript.

Notes

The authors declare no competing financial interest.

References

(1) Kojima, A.; Teshima, K.; Shirai, Y.; Mijasaka, T. Organometal Halide Perovskites as Visible-Light Sensitizers for Photovoltaic Cells. *J. Am. Chem. Soc* **2009**, *131*, 6050–6051.

(2) NREL. Best Research-Cell Efficiency Chart https://www.nrel.gov/pv/cell-efficiency.html.

(3) Kim, Y.; Cho, H.; Lee, T. Metal Halide Perovskite Light Emitters. *PNAS* **2016**, *113*, 11694–11702.

(4) Quan, L. N.; Rand, B. P.; Friend, R. H.; Mhaisalkar, S. G.; Lee, T. W.; Sargent, E. H. Perovskites for Next-Generation Optical Sources. *Chem. Rev.* **2019**, *119*, 7444–7447.

(5) Mccall, K. M.; Stoumpos, C. C.; Kontsevoi, O. Y.; Alexander, G. C. B.; Wessels, B. W.; Kanatzidis, M. G. From 0D $Cs_3Bi_2I_9$ to 2D $Cs_3Bi_2I_6Cl_3$ Dimensional Expansion Induces Direct Bandgap but Enhances Electron-Phonon Coupling. *Chem. Mater* **2019**, *31*, 2644–2650.

(6) Jiang, F.; Yang, D.; Jiang, Y.; Liu, T.; Zhao, X.; Ming, Y.; Luo, B.; Qin, F.; Fan, J.; Han, H.; Zhang, L.; and Zhou, Y. Chlorine-Incorporation-Induced Formation of the Layered Phase for Antimony-Based Lead-Free Perovskite Solar Cells. *J. Am. Chem. Soc* **2018**, *140*, 1019–1027.

(7) Morgan, E. E.; Mao, L.; Teicher, S. M. L.; Wu, G.; Seshadri, R. Tunable Perovskite-Derived Bismuth Halides: $Cs_3Bi_2(Cl_{1-x}I_x)_9$. *Inorg. Chem.* **2020**, *59*, 3387–3393.

(8) Slavney, A. H.; Hu, T.; Lindenberg, A. M.; Karunadasa, H. I. A Bismuth-Halide Double Perovskite with Long Carrier Recombination Lifetime for Photovoltaic Applications. *JACS* **2016**, *138*, 2138–2141.

(9) McClure, E. T.; Ball, M. R.; Windl, W.; Woodward, P. M. Cs_2AgBiX_6 (X = Br, Cl): New Visible Light Absorbing, Lead-Free Halide Perovskite Semiconductors. *Chem. Mater.* **2016**, *28*, 1348–1354.

(10) Gray, M. B.; Majher, J. D.; Strom, T. A.; Woodward, P. M. Broadband White Emission in $Cs_2AgIn_{1-x}Bi_xCl_6$ Phosphors. *Inorg. Chem* **2019**, *58*, 13403–13410.

(11) Majher, J. D.; Gray, M. B.; Strom, T. A.; Woodward, P. M. $Cs_2NaBiCl_6:Mn^{2+}$: A New

Orange-Red Halide Double Perovskite Phosphor. *Chem. Mater.* **2019**, *31*, 1738–1744.

(12) Kim, S. W.; Zhang, R.; Halasyamani, P. S.; Hayward, M. A. $K_4Fe_3F_{12}$: An Fe^{2+}/Fe^{3+} Charge-Ordered, Ferrimagnetic Fluoride with a Cation-Deficient, Layered Perovskite Structure. *Inorg. Chem.* **2015**, *54*, 6647–6652.

(13) Vargas, B.; Ramos, E.; Perez-Gutierrez, E.; Alonso, J. C.; Solis-Ibarra, D. A Direct Bandgap Copper–Antimony Halide Perovskite. *J. Am. Chem. Soc* **2017**, *139*, 9116–9119.

(14) Vargas, B.; Torres-Cadena, R.; Rodríguez-Hernández, J.; Gembicky, M.; Xie, H.; Jiménez-Mier, J.; Liu, Y.-S.; Menéndez-Proupin, E.; Dunbar, K. R.; Lopez, N.; Olalde-Velasco, P.; Solis-Ibarra, D. Optical, Electronic and Magnetic Engineering of <111> Layered Halide Perovskites. *Chem. Mater.* **2018**, *30*, 5315–5321.

(15) Vargas, B.; Torres-Cadena, R.; Reyes-Castillo, D. T.; Rodríguez-Hernández, J.; Gembicky, M.; Menendez-Proupin, E.; Solis-Ibarra, D. Chemical Diversity in Lead-Free, Layered Double Perovskites: A Combined Experimental and Computational Approach. *Chem. Mater.* **2020**, *32*, 424–429.

(16) Lin, Y.-P.; Hu, S.; Xia, B.; Fan, K.-Q.; Gong, L.-K.; Kong, J.-T.; Huang, X.-Y.; Xiao, Z.; Du, K.-Z. Material Design and Optoelectronic Properties of Three-Dimensional Quadruple Perovskite Halides. *J. Phys. Chem. Lett.* **2019**, *10*, 5219–5225.

(17) Holzapfel, N. P.; Majher, J. D.; Strom, T. A.; Moore, C. E.; Woodward, P. M. $Cs_4Cd_{1-x}Mn_xBi_2Cl_{12}$—A Vacancy-Ordered Halide Perovskite Phosphor with High-Efficiency Orange-Red Emission. *Chem. Mater.* **2020**, *32*, 3510–3516.

(18) Vargas, B.; Reyes-Castillo, D. T.; Coutino-Gonzalez, E.; Sánchez-Aké, C.; Ramos, C.; Falcony, C.; Solis-Ibarra, D. Enhanced Luminescence and Mechanistic Studies on Layered Double-Perovskite Phosphors: $Cs_4Cd_{1-x}Mn_xBi_2Cl_{12}$. *Chem. Mater.* **2020**, *32*, 9307–9315.

(19) Yang, H.; Shi, W.; Cai, T.; Hills-Kimball, K.; Liu, Z.; Dube, L.; Chen, O. Synthesis of Lead-Free $Cs_4(Cd_{1-x}Mn_x)Bi_2Cl_{12}$ ($0 \leq x \leq 1$) Layered Double Perovskite Nanocrystals with Controlled Mn-Mn Coupling Interaction. *Nanoscale* **2020**, *12*, 23191–23199.

(20) Xu, J.; Liu, J.-B.; Wang, J.; Liu, B.-X.; Huang, B. Prediction of Novel *p* -Type Transparent Conductors in Layered Double Perovskites: A First-Principles Study. *Adv. Funct. Mater.* **2018**, *28*, 1800332.

(21) Hu, S.; Xia, B.; Lin, Y.; Katase, T.; Fujioka, J.; Kamiya, T.; Hosono, H.; Du, K.; Xiao, Z. p-Type Transparent Quadruple Perovskite Halide Conductors: Fact or Fiction? *Adv. Funct. Mater.* **2020**, *30*, 1909906.

(22) Cohelo, A. TOPAS-Academic. *Powder Diffr.* **2007**, 312–317.

(23) Gray, M. B.; McClure, E. T.; Woodward, P. M. $Cs_2AgBiBr_{6-x}Cl_x$ Solid Solutions-Band Gap Engineering with Halide Double Perovskites. *J. Mater. Chem. C* **2019**, *7*, 9686–9689.

(24) Tilley, R. J. D. Perovskites: Structure-Property Relationships. *John Wiley Sons, Ltd* **2016**, 79–122.

(25) Madden, P. A.; Wilson, M. “Covalent” Effects in ‘ionic’ Systems. *Chem. Soc. Rev.* **1996**, *25*, 339–350.

(26) Chang, J.-H.; Doert, T.; Ruck, M. Structural Variety of Defect Perovskite Variants $M_3E_2X_9$ (M = Rb, Tl, E = Bi, Sb, X = Br, I). *Z. Anorg. Allg. Chem* **2016**, *642*, 736–748.

(27) Fabini, D. H.; Seshadri, R.; Kanatzidis, M. G. The Underappreciated Lone Pair in Halide Perovskites Underpins Their Unusual Properties. *MRS Bull.* **2020**, *45*, 467–477.

(28) Li, J.; Yu, Q.; He, Y.; Stoumpos, C. C.; Niu, G.; Trimarchi, G.; Guo, H.; Dong, G.; Wang, D.; Wang, L.; Kanatzidis, M. $Cs_2PbI_2Cl_2$, All-Inorganic Two-Dimensional Ruddlesden-Popper Mixed Halide Perovskite with Optoelectronic Response. *J. Am. Chem. Soc.* **2018**, *140*, 11085–11090.

(29) Rawl, R.; Lee, M.; Choi, E. S.; Li, G.; Chen, K. W.; Baumbach, R.; dela Cruz, C. R.; Ma, J.; Zhou, H. D. Magnetic Properties of the Triangular Lattice Magnets $A_4B'B_2O_{12}$ (A=Ba, Sr, La; B'=Co, Ni, Mn; B=W, Re). *Phys. Rev. B* **2017**, *95*, 174438.

TOC Graphic:

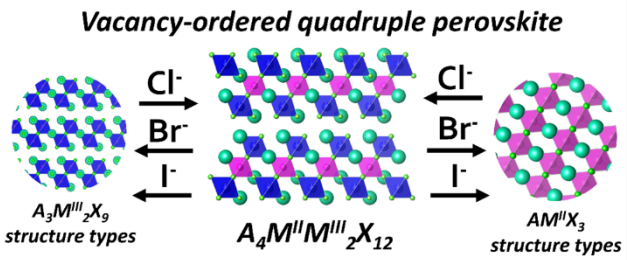
Vacancy-ordered quadruple perovskite
Cl-
Br-
I-
Cl-
Br-
I-
A3MIII2X9
structure types
A4MIIMIII2X12
AMIIX3
structure types